Modelling of Acoustic Liners Consisting of Helmholtz Resonators Coupled with a Second Cavity by Flexible Walls

Fleming Kohlenberg*
Technical University of Berlin, 10623 Berlin, Germany

Anita Schulz†
HTW Berlin University of Applied Sciences, 12469 Berlin, Germany

Lars Enghardt‡
Technical University of Berlin, 10623 Berlin, Germany

Karsten Knobloch§
German Aerospace Center (DLR), 10623 Berlin, Germany

Acoustic liners are an effective way to dampen aircraft noise. Conventional single-degree-of-freedom liners consist of a perforated facesheet backed with a honeycomb structure and a rigid end plate. Their damping excels near their resonance frequency which is anti-proportional to the cavity depth ($\lambda/4$-resonator) or the cavity volume (Helmholtz resonator). However, this is a challenge for low-frequency noise with long wavelengths due to the limited installation space. We therefore propose a resonator in which the back cavity is divided into two cavities by a flexible plate. The aim is to combine the damping mechanisms of the Helmholtz resonator with the material damping of the flexible plate. With carefully chosen parameters, this flexible plate resonates well below the Helmholtz frequency. We derived an analytic model based on waveguide theory to predict the impedance of the resonator concept. The Helmholtz equation was solved to (numerically) determine the scattering coefficients of a channel section in which one wall is lined with the predicted resonator impedance. The predicted dissipation agreed well with experimental data from measurements at the aero-acoustic wind tunnel DUCT-R.

Nomenclature

A, A_{wall}	=	area, area covered by the cavity wall of one resonator cell
c	=	speed of sound
D	=	flexural rigidity

*PhD candidate, Technical University of Berlin, Institute of Fluid Dynamics and Technical Acoustics, 10623 Berlin, Germany, AIAA Student Member, fleming.kohlenberg@dlr.de
†Professor, HTW Berlin University of Applied Sciences, Dept. of Energy and Information, 12469 Berlin, Germany
‡Professor, Technical University of Berlin, Institute of Fluid Dynamics and Technical Acoustics, 10623 Berlin, Germany, AIAA Senior Member
§Scientist, DLR Engine Acoustics, Institute of Propulsion Technology, German Aerospace Center, 10623 Berlin, Germany, AIAA Member
Presented as Paper 2824 at the 28th AIAA/CEAS Aeroacoustics 2022 Conference, Southampton, UK, June 14-17 2022

E	=	Young's modulus
h	=	plate thickness
I, I_m	=	area moment of inertia, modified Bessel function of the first kind of m^{th} order
J_m	=	Bessel function of the first kind of m^{th} order
K_1	=	modal stiffness
k	=	wave number
l	=	length
M_1	=	modal mass
N	=	number of openings per cavity
p	=	sound pressure
Δp	=	acoustic pressure difference
Pr	=	Prandtl number
R, R_p	=	energy reflection, outer plate radius
r	=	reflection factor
r_cav	=	(equivalent) radius of the cavity
r_neck	=	radius of the neck in the facesheet
S	=	plate surface
s	=	shear wave number
T	=	energy transmission
U	=	perimeter
$v, \hat{v}$	=	velocity, velocity amplitude
W	=	wave impedance
x	=	deflection
$Y, Y_\mathrm{bl,th}$	=	admittance, thermal boundary layer admittance
$Z, Z_\mathrm{m,in}, Z_\mathrm{m,out}$	=	acoustic impedance, - of the inner attached mass, - of the outer attached mass
γ	=	heat capacity ratio
$\delta_\mathrm{a}, \delta_\mathrm{m}$	=	thickness of the acoustic boundary layer, end correction length
Δ	=	energy dissipation
ζ	=	normalized impedance
η	=	loss factor
θ, χ	=	normalized resistance, normalized reactance
$\lambda, \lambda_{m,n}$	=	acoustic wave length, frequency parameter for each eigenform

$\nu_{\mathrm{kin}}, \nu_{\mathrm{PR}}$	=	kinematic viscosity, Poisson's ratio
ξ	=	ratio of hole area to reference area
ρ	=	density
σ	=	open area ratio
ϕ	=	angle
ψ	=	eigenmode
ψ_{Fock}	=	Fock function to account for hole interactions
ω	=	angular frequency
Subscripts		
cav, cav_1, cav_2	=	cavity, main cavity, second cavity
neck	=	facesheet opening
0	=	ambient
p	=	plate
n, m	=	index
PH	=	plate holder
cc	=	circular clamped

I. Introduction

The reduction of aircraft noise is an ongoing challenge with ever increasing demands for quieter flights. Aircraft noise can be subdivided into airframe and propulsion noise. In the past, significant noise reduction of the latter was achieved by cut-off design for rotor-stator-interactions and by increasing the bypass-ratio of the turbofan engine – a trend which is expected to continue. A higher bypass-ratio enables the operation of the fan with reduced speed which leads to noise with lower frequency components of broader bandwidth. This design approach is beneficial to tackle the origin of propulsion noise, but challenging for further sound attenuation by liners. Conventional liners currently in use usually consist of a perforated facesheet with a honeycomb structure underneath [1]. Their capability to dampen sound waves with long wavelengths is limited; however, as they need more cavity space to achieve this. Due to drag and weight restrictions, the installation space in the nacelle is limited and consequently, deeper cavities are not an option. Therefore, new advanced liner technologies are needed to tackle this low-frequency noise.

Conventional liners are usually modelled as a Helmholtz resonator, which is a rigid cavity filled with a compressible fluid such as air and a neck. For wavelengths much greater than the system's dimensions, the Helmholtz resonator is often modeled by combining lumped elements. In this case, the cavity is regarded as a spring and the neck as a mass

[2], acting with a Single-Degree-Of-Freedom (SDOF). The viscothermal losses inside the neck are modelled as an equivalent resistance. Contrary, viscothermal losses inside the cavity are usually neglected, since the main dissipation mechanisms are concentrated in the neck [3]. The combination of a neck with a cavity allows a resonance frequency lower than a resonator only consisting of a cavity ($\lambda/4$-resonator). This, however, comes at the cost of a smaller sound absorption bandwidth. A straightforward way to regain broad noise reduction is by combining multiple distinctive SDOF resonators for example with variable depth [4]. This concept can be extended by using bent chambers or facesheets with attached tubes [5]. A different approach is to design a liner with multiple coupled resonators, therefore acting with Multi-Degrees-of-Freedom (MDOF). A common approach is the subdivision of the cavity with additional elements such as mesh-material [5–7] or perforations [8–10].

One way to enable noise reduction at lower frequencies than conventional liners, is to combine hard walled Helmholtz resonators with additional mechanical elements such as membranes or plates. These mechanical elements have the advantage, that their individual resonance frequencies can be tuned independently of the Helmholtz resonator. The main difference between membranes and plates is the physical principle of their elasticity. Membranes are elastic because of the applied tension, similar to a drum. Contrary, plates draw their elasticity from their flexural rigidity, similar to the top plate of a classical guitar. A combination, for example a thin plate with applied tension, is sometimes called a foil [11]. Even if a rigorous prediction of such a foil's motion is complicated, a rule of thumb is that positive pre-stress seems to stiffen the plate, while a negatively pre-stressed plate appears to be more flexible [12]. Plates are often treated in building acoustics with respect of sound transmission through walls. An important aspect in that research field is the coincidence frequency, where the projected incoming sound wavelength matches the bending wavelength of the plate. However, since flexible plates used inside resonators for aero-acoustic damping are considerably thinner than brick walls, the coincidence effect is in most cases negligible in the context of liners.

Many researchers investigated the effect of combining resonators with membranes. Griffin et al. [13] used a thin membrane to couple two cavities in a liner and measured the transmission loss of the system. They found multiple transmission loss peaks and concluded that the membrane provided a coupling and alteration of the resonators cavity volume. They developed a mechanical system with lumped elements to predict the transmission loss by modeling the membrane as a piston vibrating only in its first mode. Zhao et al. [14] extended the concept by modeling a similar parallel-coupled system using Green's functions and included higher membrane modes in the process. They found that the combined resonance frequencies are distinct compared to the uncoupled resonances. They also found that altering the membranes stiffness had a big effect on additional transmission loss peaks.

Mi and Yu [15] combined Helmholtz resonators, a circular membrane and an U-shaped duct, acting as a Herschel-Quincke tube, to create a sophisticated MDOF resonator. The tensioned membrane was implemented as a flexible back plate for two Helmholtz resonators attached to the same waveguide. They proposed an analytic model based on travelling plane waves and a modal expansion approach of the membrane and compared their transmission loss with

finite element simulations. Apart from the subsystems' resonances (Helmholtz resonance, membrane resonance and Herschel-Quincke resonance), they found an additional low-frequency transmission loss peak which they attributed to the structural-acoustic coupling.

Recently, Dodge et al. [16] included a membrane made of a dielectric elastomer in their liner. They used the dielectric material property to change the membranes compliance to create a tunable resonator with low-frequency damping. The impedance was modelled by a lumped element approach and good agreement with experimental data was found. However, the inclusion of the electric effects on the impedance remained a challenge.

A difficulty when coupling resonators with membranes is the fact that their acoustic behavior strongly depends on the membrane's applied tension which is challenging to determine, to control and may change over time. This disadvantage is overcome when using flexible plates instead of membranes.

In previous studies, flexible plates were often used as flexible back plates to improve attenuation. Horowitz et al. [17] swapped the rigid backplate of a Helmholtz resonator with an aluminum diaphragm to add degrees of freedom to the system. The system was modelled as an equivalent circuit using lumped elements. They determined an equivalent impedance of their clamped circular end plate by an energy analysis of the total distributed potential and kinetic energy stored in the static deflection. Material losses were not analytically modelled but added as an additional resistance to fit the experimental data. Liu et al. [18] later extended the model with a piezoelectric composite back plate to construct a tunable resonator. A similar approach was used by Nudehi et al. [19] who also investigated the impact of a flexible back plate on a Helmholtz resonator. They modelled the system with lumped elements of the resonator neck and cavity and an equivalent receptance of the flexible plate. Their study suggested the possibility to lower the system's main transmission loss peak in comparison to a resonator with a rigid back wall.

More recently, flexible plates have also been investigated as a mean to couple multiple resonator chambers. Knobloch et al. [20, 21] replaced the rigid side walls of a liner segment with flexible walls to couple cavities and subsequently enable broadband damping. In their studies, active cells with a connection to the duct were coupled with inactive cells by flexible walls. They proved that the concept of integrating flexible walls is beneficial for low-frequency broadband damping. Liu et al. [22] coupled Helmholtz resonators with a piezoelectric composite sheet to construct an acoustic energy harvester. The diaphragm was excited by the phase difference between adjacent Helmholtz resonators with different resonance frequencies.

This phase difference can also be achieved by coupling a Helmholtz resonator with a second cavity by a flexible plate. Sanada and Tanaka [23] constructed a MDOF resonator composed of a perforated plate and two cavities coupled via a clamped circular plate. They modelled the system by combining lumped elements of the air in the perforated plate, the cavities and an equivalent impedance of the flexible panel. The fundamental characteristics of the absorber were investigated using dimensionless parameters. To achieve a broad attenuation, they suggested a lightweight panel with a loss factor as high as possible and a high porosity of the perforated plate. However, they did not model the

resonator's resistance neither in the perforated front plate nor in the cavity but determined the resistance experimentally. Additionally, their study was restricted to direct sound incidence.

In the present study we propose a model of a Helmholtz resonator coupled to a second cavity with a flexible plate. The resonator is viewed as one cell of a liner. We take into account the viscoelastic losses inside the flexible plate, as well as viscothermal losses both in the neck and inside the cavity. Hence, multiple damping mechanisms are combined in the resonator concept proposed here. Elastomers are reasonable candidates for the plate material, as they offer high inherent mechanical losses. The proposed model is an extended combination of the models proposed by Sanada and Tanaka [23] and Schulz [24], in which we combine one dimensional waveguide theory with lumped elements. The impedances (or their reciprocals, the admittances) of the individual elements are connected alternately in series or in parallel and are spatially transformed throughout the resonator. The idea is to start at the thermal boundary layer at the back of the resonator and use a waveguide model to spatially transform that impedance through the resonator up to the flow channel. The flexible plate is modelled as an equivalent impedance and integrated into the waveguide model. The result is an impedance of the resonator system, which is used as a boundary condition in a numerical simulation that solves the Helmholtz equation to predict scattering coefficients of the duct section with the resonator system attached to one side. These are compared to results from measurements we conducted at the DLR liner test facility DUCT-R.

The first section treats the case of a simple Helmholtz resonator without a flexible panel (see Fig. 1) which is connected to the flow channel by a perforated plate with multiple openings per cavity. The modelling of the flexible plate and a coupled Helmholtz resonator with a second cavity (see Fig. 2) is introduced in Section III. The mechanical element serves as a coupling between the main cavity with a second cavity with viscoelastic losses, thus providing an additional damping mechanism. The experimental setup to validate the model is specified in the fourth section. The results, which include a comparison between predicted and measured scattering coefficients are presented in the fifth section. Finally, a conclusion and an outlook for future research is drawn.

II. Impedance model of the SDOF Helmholtz resonator

The following model is an adaption of a SDOF Helmholtz resonator model developed previously by the authors [24, 25]. Figure 1 shows the cross-sectional sketch of one resonator cell of the liner to be regarded. The liner is considered as a periodic array of equal such resonator cells. The cavity with length l_{cav} and diameter $2r_{\mathrm{cav}}$ is coupled to the outer acoustic field by N equal circular, straight, and sharp-edged orifices with radius r_{neck} and neck length l_{neck}. The openings are equally distributed across the front wall.

The following workflow is used to calculate the impedance of the resonator system:

1) We start at the rear wall of the cavity ($y = 0$) where the wall is sound-hard and the wall admittance is zero. Hence, the normal incidence impedance only consists of the admittance of the thermal boundary layer (blue line

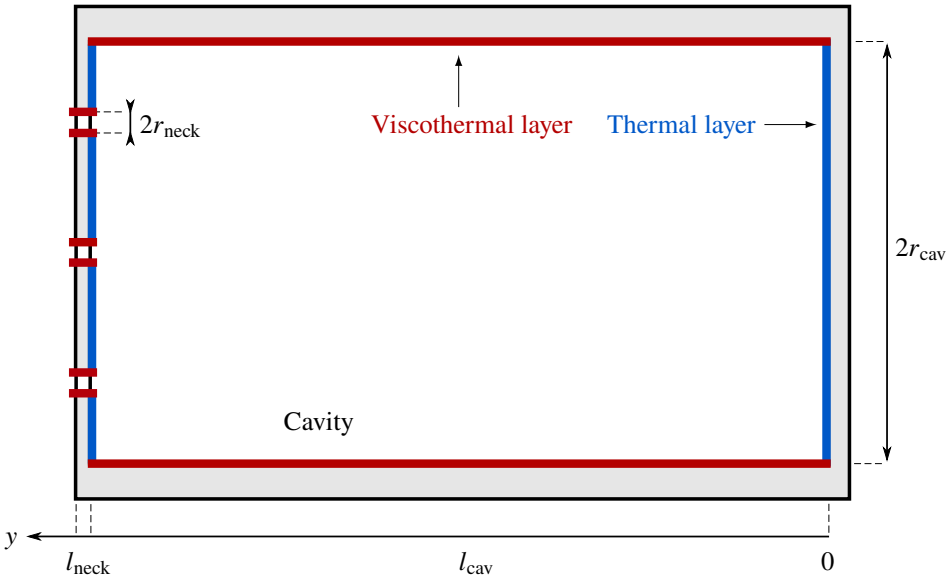

Fig. 1 Sketch of a circular Helmholtz resonator with viscous and thermal layers

in Fig. 1) and according to [26] reads

$$Z_1 = -\frac{p}{v}\bigg|_{y=0} = \frac{1}{Y_{\text{bl,th}}} = (1-\mathrm{i})\,\frac{\rho_0 c}{k_0 \delta_\text{a}}\,\frac{\sqrt{Pr}}{\gamma-1} \tag{1}$$

where p is the sound pressure, v is the y-component of the particle velocity, ρ_0 is the ambient density of air, c is the speed of sound, $k_0 = \omega/c$ is the free field wave number, γ is the heat capacity ratio, $\delta_\text{a} = \sqrt{2\nu_\text{kin}/\omega}$ is the thickness of the acoustic boundary layer, Pr is the Prandtl number and ν_kin the kinematic viscosity. The negative sign in Eq. (1) accounts for the definition of the wall impedance with the normal particle velocity v pointing into the wall (i.e. in negative y-direction, see Fig. 1). Note that the effect of the viscous boundary layer at the back wall can be neglected since the wall-parallel component of the particle velocity (which would have to be decelerated by the friction effects) vanishes in front of the hard rear wall of the cavity.

2) The impedance Z_1 (at $y = 0$) is transformed spatially to the position $y = l_\text{cav}$ of the backside of the front plate. This step takes into account the one dimensional wave propagation in y-direction in the cavity and the effect of the lateral viscous and thermal boundary layers (marked with red lines in Fig. 1).* The presence of the viscothermal boundary layers leads to a modified wavenumber for the (almost plane) waves traveling back and forth in the cavity. This modified wavenumber for wide wave guides reads

$$k_\text{cav} = k_0\left[1 + \frac{1-\mathrm{i}}{4}\left(1+\frac{\gamma-1}{\sqrt{Pr}}\right)\frac{U_\text{cav}}{A_\text{cav}}\delta_\text{a}\right] \tag{2}$$

*Note that the influence of the viscous boundary layer depends on the particle velocity amplitude and is only substantial when the cavity depth is comparably large to the wavelength, due to the rigid boundary condition at the back wall.

where A_{cav} is the cross sectional area of the cavity and U_{cav} is the corresponding perimeter.[†] Note that in the case of a cylindrical cavity $U/A = 2/r_{\mathrm{cav}}$.

The lateral boundary layers in the cavity also modify the wave impedance of the cavity sound field, which is defined as the ratio between acoustic pressure and wall-parallel particle velocity, averaged over the cavity's cross section [24]:

$$W_{\mathrm{cav}} = -\frac{p}{v}\bigg|_{\mathrm{cav}} = (\rho_0 c)/\left[\frac{k_{\mathrm{cav}}}{k_0}\left(1 - \frac{(1-\mathrm{i})}{2}\frac{U_{\mathrm{cav}}}{A_{\mathrm{cav}}}\delta_{\mathrm{a}}\right)\right] \tag{3}$$

With the two prerequisites Eqs. (2) and (3), the impedance at $y = l_{\mathrm{cav}}$ is

$$Z_2 = W_{\mathrm{cav}}\frac{1 + r_1\,\mathrm{e}^{-2\mathrm{i}k_{\mathrm{cav}}l_{\mathrm{cav}}}}{1 - r_1\,\mathrm{e}^{-2\mathrm{i}k_{\mathrm{cav}}l_{\mathrm{cav}}}} \tag{4}$$

where the reflection factor of the rigid back wall with a thermal boundary layer is

$$r_1 = \frac{Z_1 - W_{\mathrm{cav}}}{Z_1 + W_{\mathrm{cav}}} \tag{5}$$

3) At $y = l_{\mathrm{cav}}$ the effect of the compressible air in the cavity (expressed by Z_2) has to be superimposed with the effect of the thermal boundary layer at the inner side of the front plate (left blue lines in Fig. 1). This corresponds to an addition of the admittance $1/Z_2$ and the thermal boundary layer admittance $Y_{\mathrm{bl,th}}$ in Eq. (1)) since the two kinds of acoustic compliances are driven by the same pressure. This gives

$$Z_3 = \frac{1}{Y_3} \quad \text{with} \quad Y_3 = \frac{1}{Z_2} + Y_{\mathrm{bl,th}}\left(1 - \frac{N\pi r_{\mathrm{neck}}^2}{A_{\mathrm{cav}}}\right) \tag{6}$$

where N denotes the number of openings per cavity. On the right hand side of Eq. (6), $Y_{\mathrm{bl,th}}$ is corrected by an area ratio which accounts for the effective wall area where the thermal boundary layer is applied (the opening areas are cutout).

4) The total impedance of the cavity Z_3 now has to be connected to the impedance of the openings which act in parallel. The impedance of a single opening mainly comprises the friction at the sidewall of the opening and the acceleration of the mass within the neck of the opening, including the inner and outer attached mass. The parallel connection of the openings is expressed by the fact that each (evenly spaced) opening is described by an equal wall surface assigned to it. In case of the inner side of the front plate this unit area is simply A_{cav}/N. The cross-sectional jump between this inner unit area and the area of one orifice changes the distribution of acoustic particle velocity and hence the admittance. This is taken into account by an area transformation $\pi r_{\mathrm{neck}}^2/(A_{\mathrm{cav}}/N)$.

[†]Equation (2) is valid when the boundary layers are far away from each other and corresponds to the "Kirchhoff 'wide tube'" solution [27, 28]. It is applicable when high shear wave numbers $s = r\sqrt{\omega/\nu_{\mathrm{kin}}} > 3$ are present. A shear wave number of three corresponds to the situation of an acoustic wave with 200 Hz in a cylinder with radius $r = 0.33$ mm in air at ambient conditions.

Next, the inner attached mass $Z_{\mathrm{m,in}}$, which accounts for near fields around the inner cross-sectional jump at the opening, is added:

$$Z_4 = \frac{\pi r_{\mathrm{neck}}^2}{A_{\mathrm{cav}}/N} Z_3 + Z_{\mathrm{m,in}} \tag{7}$$

It is well known [3] that the (one-sided) additional mass can be described by the impedance of a short open tube (length $\ll \lambda$) with the radius r_{neck}. For a circular opening in an infinite plate this gives an end correction of $\delta_{\mathrm{m}} = 8/(3\pi) r_{\mathrm{neck}} \approx 0.85 r_{\mathrm{neck}}$ and the corresponding impedance would be (in the inviscid case) $Z_{\mathrm{m,in}} = \mathrm{i} k_0 \rho c \delta_{\mathrm{m}}$. However, this end correction is diminished by the side walls and in our case particularly by neighboring openings. Ingard [3], by means of an inviscid theory, has derived the end correction for a circular resonator opening in a circular or rectangular cross-sectional cavity. The effect of multiple openings above one cavity can be expressed by mirror sources which act like virtual cavity walls at the rims of the before mentioned unit area of each opening. The effect of hole interactions can be accounted for by the Fock function ψ_{Fock} [29].[‡] Alternatively, for moderate ratios $\xi_{\mathrm{in}} = \sqrt{\pi r_{\mathrm{neck}}^2/(A_{\mathrm{cav}}/N)} < 0.4$ (which is fulfilled in most practical liner applications with small porosities), the end correction can be approximated after Ingard [3] by $\delta_{\mathrm{m}} = 8/(3\pi)(1 - 1.25\,\xi_{\mathrm{in}}) r_{\mathrm{neck}}$. The impedance of the inner additional mass ,consequently, is

$$Z_{\mathrm{m,in}} = \mathrm{i} \frac{8}{3\pi} \psi_{\mathrm{Fock}}(\xi_{\mathrm{in}}) r_{\mathrm{neck}} k_{\mathrm{neck}} W_{\mathrm{neck}} \approx \mathrm{i} \frac{8}{3\pi} (1 - 1.25\,\xi_{\mathrm{in}}) r_{\mathrm{neck}} k_{\mathrm{neck}} W_{\mathrm{neck}} \tag{8}$$

The wavenumber k_{neck} and the wave impedance W_{neck} of the wave propagation within the opening (seen as a one dimensional waveguide) can be adopted from Eq. (2) and Eq. (3) but with $U_{\mathrm{neck}}/A_{\mathrm{neck}} = 2/r_{\mathrm{neck}}$ instead of $U_{\mathrm{cav}}/A_{\mathrm{cav}}$.

5) Next, the neck mass impedance is added by a spatial transform of the impedance Z_4 through the opening, i.e. from $y = l_{\mathrm{cav}}$ to $y = l_{\mathrm{cav}} + l_{\mathrm{neck}}$ in Fig. 1. The same procedure as in step two can be used which yields

$$Z_5 = W_{\mathrm{neck}} \frac{1 + r_2\, \mathrm{e}^{-2\mathrm{i} k_{\mathrm{neck}} l_{\mathrm{neck}}}}{1 - r_2\, \mathrm{e}^{-2\mathrm{i} k_{\mathrm{neck}} l_{\mathrm{neck}}}} \tag{9}$$

where the reflection factor at the inner end of the opening ($y = l_{\mathrm{cav}}$) is

$$r_2 = \frac{Z_4 - W_{\mathrm{neck}}}{Z_4 + W_{\mathrm{neck}}} \tag{10}$$

6) At the exterior end of the opening, the outer additional mass impedance $Z_{\mathrm{m,out}}$ has to be added to Z_5. In addition, the cross-sectional jump of the total impedance (from the opening area to the outer unit wall area) is taken into account by an area transformation. This has already been used in step 4 (in the reverse manner). However, the

[‡]Note that Fock [29] introduced a correction term for the *conductance* of a hole, which is inverse proportional to the impedance of such. Consequently, the original function was defined as the inverse of ψ_{Fock} used in this work. ψ_{Fock} shortens the additional length.

outer unit wall area, i.e. the area element which can be assigned to each single opening and which in a sum over all area elements covers the total liner surface, is slightly increased (compared to the inner unit area) because of the finite thickness of the cavity walls. Let A_{wall} be the area which is covered by the cavity walls of one representative resonator cell of the liner (the liner is regarded as a periodic array of equal such resonators). Then the acoustic flux due to the cross-sectional jump has to be "distributed" from the area of one opening to the outer unit wall area $(A_{\mathrm{cav}} + A_{\mathrm{wall}})/N$. Thus the total impedance of a liner with N circular openings above one resonator cavity reads:

$$Z_6 = (Z_5 + Z_{\mathrm{m,out}}) \frac{(A_{\mathrm{cav}} + A_{\mathrm{wall}})/N}{\pi r_{\mathrm{neck}}^2} \tag{11}$$

For the derivation of the outer attached mass impedance $Z_{\mathrm{m,out}}$ the same argument as in step 4 applies, but accordingly the outer unit area has to be used. The length ratio ξ_{in} in Eq. (8) hence is replaced by $\xi_{\mathrm{out}} = \sqrt{\pi r_{\mathrm{neck}}^2/((A_{\mathrm{cav}} + A_{\mathrm{wall}})/N)}$.

III. Impedance model of the MDOF Helmholtz resonator with a second cavity coupled by a flexible plate

In this section the equivalent impedance of a flexible plate is derived similar to [23]. This impedance is then combined with the model introduced in the previous section to obtain a model of a Helmholtz resonator with a flexible plate, depicted in Fig. 2. We assume the plate to be round, homogeneous and thin compared to its length. As the plate is excited by acoustical pressure differences, the deflections are assumed to be small. The corresponding differential equation for the plate's motion then reads:

$$D\nabla^4\{x_{\mathrm{p}}(r,t)\} + \rho_{\mathrm{p}} h \frac{\partial^2 x_{\mathrm{p}}(r,t)}{\partial t^2} = \Delta p \, \mathrm{e}^{\mathrm{i}\omega t} \tag{12}$$

In Eq. (12) ρ_{p} is the density of the plate, h is the plate thickness, x_{p} is the deflection of the plate, Δp is pressure difference due to the exciting acoustic wave. The flexural rigidity D for a thin plate is given by

$$D = (1 + \mathrm{i}\eta) EI = (1 + \mathrm{i}\eta) \frac{E h^3}{12(1 - \nu_{\mathrm{PR}}^2)} \tag{13}$$

where η denotes the loss factor, E denotes Young's modulus, I denotes the area moment of inertia and ν_{PR} denotes Poisson's ratio. In Eq. (12), the Laplacian Δ is applied twice: $\nabla^4 = \Delta\Delta$, which results in a partial differential equation of fourth order.[§] Due to the harmonic excitation, the plate's velocity is assumed to be harmonic as well, yielding

[§]This is in contrast to the motion of a membrane, where the corresponding partial differential equation only contains the second derivative with respect to the deflection.

$v_\mathrm{p}(r,t) = \hat{v}_\mathrm{p}(r)\,\mathrm{e}^{\mathrm{i}\omega t} = \mathrm{i}\omega\hat{x}_\mathrm{p}(r)\,\mathrm{e}^{\mathrm{i}\omega t}$. Eq. (12) can therefore be written as

$$\frac{D}{\mathrm{i}\omega}\nabla^4\{\hat{v}_\mathrm{p}(r)\} + \mathrm{i}\omega\rho_\mathrm{p}h\hat{v}_\mathrm{p}(r) = \Delta p \tag{14}$$

The velocity of the circular plate can be expressed by the superposition of infinitely many eigenmodes ψ_n and the corresponding modal amplitudes $\hat{v}_{\mathrm{p},n}$ for each mode n as

$$\hat{v}_\mathrm{p}(r) = \sum_{n=0}^{\infty}\hat{v}_{\mathrm{p},n}\psi_n(r) \tag{15}$$

Following [30], the eigenmodes of a clamped circular plate ($\psi_\mathrm{cc}(R_\mathrm{p}) = \frac{\partial\psi_\mathrm{cc}}{\partial r}|_{R_\mathrm{p}} = 0$) with the outer radius R_p can be approximated by

$$\psi_\mathrm{cc}(r,\varphi,m,n) = \left[J_m\left(\frac{\lambda_{m,n}}{R_\mathrm{p}}r\right) - \frac{J_m\left(\lambda_{m,n}\right)}{I_m\left(\lambda_{m,n}\right)}I_m\left(\frac{\lambda_{m,n}}{R_\mathrm{p}}r\right)\right]\cos(m\varphi) \tag{16}$$

with J_m the Bessel function of the first kind of m^th order, I_m the modified Bessel function of the first kind of m^th order and $\lambda_{m,n}$ a frequency parameter of each eigenform and the angle φ. The frequency parameter of a clamped circular plate can be calculated using the transcendental equation

$$\frac{J_m(\lambda)}{J_{m+1}(\lambda)} + \frac{I_m(\lambda)}{I_{m+1}(\lambda)} = 0 \tag{17}$$

Like in Section II, we assume that only plane waves are able to propagate inside the cavity (but outside the boundary layer). Hence, the excitation of the plate is assumed to be independent of φ. Consequently, the plate's motion is assumed to be dominated by the fundamental eigenmode of order $m, n = 0$:

$$\psi(r) = \psi_{\mathrm{cc},0}(r) = J_0\left(\frac{\lambda_0}{R_\mathrm{p}}r\right) - \frac{J_0\left(\lambda_0\right)}{I_0\left(\lambda_0\right)}I_0\left(\frac{\lambda_0}{R_\mathrm{p}}r\right) \tag{18}$$

The frequency parameter of the fundamental mode $m, n = 0$ is $\lambda_0 \approx 3.196$.[¶] Given these assumptions, combining Eq. (14) and Eq. (15) yields

$$\frac{D}{\mathrm{i}\omega}\nabla^4\{\psi(r)\}\hat{v}_\mathrm{p} + \mathrm{i}\omega\rho_\mathrm{p}h\hat{v}_\mathrm{p}\psi(r) = \Delta p \tag{19}$$

[¶]Note that Eq. (18) is also valid for a circular simply supported plate, with the sole difference that the frequency parameter of the fundamental mode is $\lambda_0(\nu_{\mathrm{PR}=0.5}) \approx 2.2831$ [31]. The fundamental eigenfrequency of a circular simply supported plate is, consequently, lower than that of a circular clamped plate.

Multiplying Eq. (19) with $\psi(r)$ and integrating over the plate's surface $S = \pi R_\mathrm{p}^2$ yields

$$\iint_S \frac{D}{\mathrm{i}\omega}\nabla^4\{\psi(r)\}\hat{v}_\mathrm{p}\psi(r) + \mathrm{i}\omega\rho_\mathrm{p}h\hat{v}_\mathrm{p}\psi(r)\psi(r)\mathrm{d}S = \iint_S \Delta p\,\psi(r)\mathrm{d}S \tag{20}$$

$$\frac{D}{\mathrm{i}\omega}\iint_S \nabla^4\{\psi(r)\}\psi(r)\mathrm{d}S + \mathrm{i}\omega\rho_\mathrm{p}h\iint_S \psi^2(r)\mathrm{d}S = \frac{\Delta p}{\hat{v}_\mathrm{p}}\iint_S \psi(r)\mathrm{d}S \tag{21}$$

The modal amplitude of the plate's velocity $\hat{v}_\mathrm{p}$ can be expressed by the mean velocity of the plate $\bar{v}_\mathrm{p}$ over the area of the plate:

$$\hat{v}_\mathrm{p} = \frac{\bar{v}_\mathrm{p}S}{\iint_S \psi(r)\mathrm{d}S} \tag{22}$$

Using Eq. (22), we finally obtain

$$\frac{1}{\mathrm{i}\omega}\underbrace{D\iint_S \nabla^4\{\psi(r)\}\psi(r)\mathrm{d}S}_{K_1} + \mathrm{i}\omega\underbrace{\rho_\mathrm{p}h\iint_S \psi^2(r)\mathrm{d}S}_{M_1} = \frac{\Delta p}{\bar{v}_\mathrm{p}}\frac{1}{S}\underbrace{\left(\iint_S \psi(r)\mathrm{d}S\right)^2}_{B} \tag{23}$$

With the introduction of

$$B = \left(\iint_S \psi(r)\mathrm{d}S\right)^2 = \left(2\pi\int_r \psi(r)r\mathrm{d}r\right)^2 \tag{24}$$

$$K_1 = D\iint_S \nabla^4\{\psi(r)\}\psi(r)\mathrm{d}S = D2\pi\int_r \nabla^4\{\psi(r)\}\psi(r)r\mathrm{d}r \tag{25}$$

$$M_1 = \rho_\mathrm{p}h2\pi\int_r \psi^2(r)r\mathrm{d}r \tag{26}$$

we express the motion of the flexible plate in terms similar to a simple oscillator with a modal mass M_1 and a modal stiffness K_1 of the fundamental mode as

$$\frac{\Delta p}{\bar{v}_\mathrm{p}} = Z_\mathrm{p} = \frac{S}{B}\left(\frac{1}{\mathrm{i}\omega}K_1 + \mathrm{i}\omega M_1\right) \tag{27}$$

To calculate Eq. (25), we take advantage of the fact that in this case the Laplacian of the eigenmode can be expressed as an eigenvalue problem:

$$\Delta\psi(r) = \left(\frac{\lambda_0}{R_\mathrm{p}}\right)^2\psi(r) \tag{28}$$

Consequently, it yields that

$$\nabla^4\psi(r) = \Delta(\Delta(\psi(r))) = \left(\frac{\lambda_0}{R_\mathrm{p}}\right)^4\psi(r) \tag{29}$$

which simplifies Eq. (25) to

$$K_1 = D2\pi \int_r \nabla^4\{\psi(r)\}\psi(r) r\mathrm{d}r = D2\pi \left(\frac{\lambda_0}{R_\mathrm{p}}\right)^4 \int_r \psi^2(r) r\mathrm{d}r \tag{30}$$

Using the simple oscillator analogy, the resonance frequency of the clamped circular plate in its fundamental mode is expressed as

$$\omega_p = \mathrm{Re}\left\{\sqrt{\frac{K_1}{M_1}}\right\} = \mathrm{Re}\left\{\left(\frac{\lambda_0}{R_\mathrm{p}}\right)^2 \sqrt{\frac{D}{\rho_\mathrm{p} h}}\right\} \tag{31}$$

which is the same eigenfrequency of a clamped circular plate as calculated in [30].

In the next step, this impedance is integrated into the resonator model of Section II. The situation is depicted in Fig. 2.

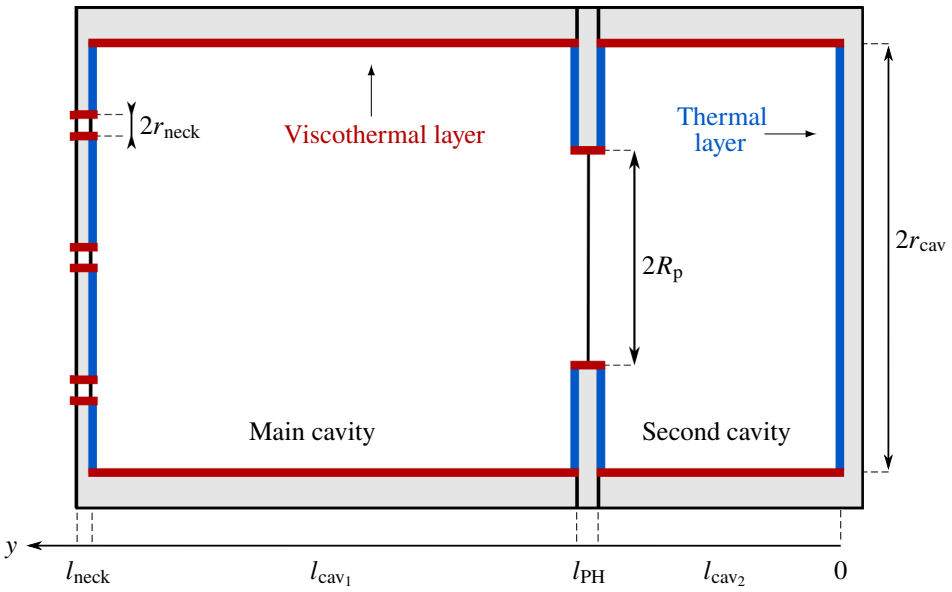

Fig. 2 Sketch of a circular Helmholtz resonator with a flexible plate inside a plate holder and a second cavity

The starting point is once again the rigid back of the cavity with a thermal boundary layer and the same reflection factor as in Eq. (5). In contrast to the previous section, the impedance in Eq. (4) is transformed spatially to the position of a plate holder at a distance of l_{cav_2}

$$Z_\mathrm{I} = W_\mathrm{cav} \frac{1 + r_1 \mathrm{e}^{-2\mathrm{i}k_\mathrm{cav} l_{\mathrm{cav}_2}}}{1 - r_1 \mathrm{e}^{-2\mathrm{i}k_\mathrm{cav} l_{\mathrm{cav}_2}}} \tag{32}$$

At the position of the plate holder, there is a parallel connection between the cavity's impedance and the impedance of the thermal boundary layer of the plate holder

$$Z_\mathrm{II} = \frac{1}{Y_\mathrm{II}} \quad \text{with} \quad Y_\mathrm{II} = \frac{1}{Z_\mathrm{I}} + Y_\mathrm{bl,th}\left(1 - \frac{S}{A_\mathrm{cav}}\right) \tag{33}$$

in which the factor S/A_{cav} ensures the continuity of the acoustic flux. The influence of the viscothermal boundary layer of the right half of the plate holder (see Fig. 2) is accounted for by

$$Z_{\mathrm{III}} = W_{\mathrm{PH}} \frac{1 + r_{\mathrm{II}}\, \mathrm{e}^{-\mathrm{i}k_{\mathrm{PH}} l_{\mathrm{PH}}}}{1 - r_{\mathrm{II}}\, \mathrm{e}^{-\mathrm{i}k_{\mathrm{PH}} l_{\mathrm{PH}}}} \quad \text{with} \quad r_{\mathrm{II}} = \frac{Z_{\mathrm{II}} - W_{\mathrm{PH}}}{Z_{\mathrm{II}} + W_{\mathrm{PH}}} \tag{34}$$

The wavenumber k_{PH} and the wave impedance W_{PH} of the wave propagation within the opening of the plate holder (seen as a one dimensional waveguide) can be adopted from Eq. (2) and Eq. (3) but with $U_{\mathrm{neck}}/A_{\mathrm{neck}} = 2/R_{\mathrm{p}}$ instead of $U_{\mathrm{cav}}/A_{\mathrm{cav}}$. The impedance of the plate as calculated in Eq. (23) is connected in series and therefore it yields:

$$Z_{\mathrm{IV}} = \frac{S}{A_{\mathrm{cav}}} Z_{\mathrm{III}} + Z_{\mathrm{p}} \tag{35}$$

The influence of the viscothermal boundary layer of the left half of the plate holder (see Fig. 2) is accounted for by

$$Z_{\mathrm{V}} = W_{\mathrm{PH}} \frac{1 + r_{\mathrm{III}}\, \mathrm{e}^{-\mathrm{i}k_{\mathrm{PH}} l_{\mathrm{PH}}}}{1 - r_{\mathrm{III}}\, \mathrm{e}^{-\mathrm{i}k_{\mathrm{PH}} l_{\mathrm{PH}}}} \quad \text{with} \quad r_{\mathrm{III}} = \frac{Z_{\mathrm{IV}} - W_{\mathrm{PH}}}{Z_{\mathrm{IV}} + W_{\mathrm{PH}}} \tag{36}$$

The effects of the cross section jump back and the effects of the thermal boundary layer of the plate holder towards the perforated plate are described by

$$Z_{\mathrm{VI}} = \frac{1}{Y_{\mathrm{VI}}} \quad \text{with} \quad Y_{\mathrm{VI}} = \frac{1}{\frac{A_{\mathrm{cav}}}{S} Z_{\mathrm{V}}} + Y_{\mathrm{bl,th}} \left(1 - \frac{S}{A_{\mathrm{cav}}}\right) \tag{37}$$

Next, the reflection factor at this position is calculated

$$r_{\mathrm{IV}} = \frac{Z_{\mathrm{VI}} - W_{\mathrm{cav}}}{Z_{\mathrm{VI}} + W_{\mathrm{cav}}} \tag{38}$$

and a spatial transformation along the main cavity is used to the backside of the perforated plate by

$$Z_2' = W_{\mathrm{cav}} \frac{1 + r_{\mathrm{IV}}\, \mathrm{e}^{-2\mathrm{i}k_{\mathrm{cav}} l_{\mathrm{cav}_1}}}{1 - r_{\mathrm{IV}}\, \mathrm{e}^{-2\mathrm{i}k_{\mathrm{cav}} l_{\mathrm{cav}_1}}} \tag{39}$$

The rest of the steps to determine the impedance of the resonator are the same as in the Helmholtz resonator case described in the previous section (Eq. (6) and following).

IV. Experimental setup

In order to validate the models we conducted several experimental investigations at the duct acoustic test rig (DUCT-R) facility of the German Aerospace Center (DLR) in Berlin. The rig is sketched in Fig. 3 and consists of two symmetrical parts with a cross section of 60 mm × 80 mm and a cut-on frequency of the first higher mode of 2142 Hz.

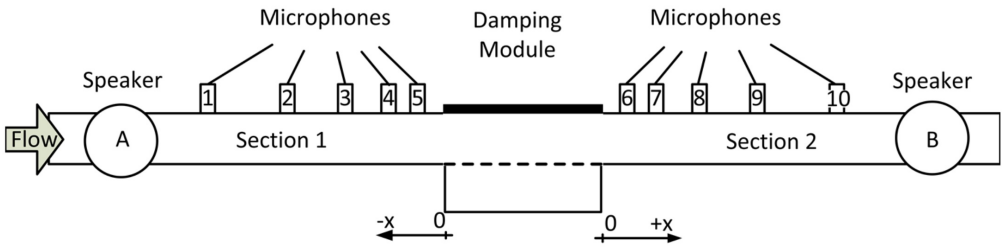

Fig. 3 Schematic view of the DUCT-R test rig

Each part is equipped with five flush mounted microphones of type 1/4" G.R.A.S. 40BP-S1 to decompose the sound field into upstream and downstream travelling sound waves in each section respectively. Their signals are recorded over a time of 5 s with an OROS 38 data acquisition system. Since we only investigated only plane travelling waves up to 2000 Hz, we set the sampling frequency to 8192 Hz and the Hann window function with an overlap of 50 % was used during post processing. The complex spectra of the microphone signals are obtained by using the method of Chung [32] with the loudspeaker input signal as a phase reference. We used five instead of two microphones to improve the accuracy of fitting the (forward and backward) travelling sound waves to the sound pressure measured at the duct wall. Additionally, a singular solution at a certain microphone spacing between two microphones is avoided. [33] The sound waves are excited either via upstream speaker A or downstream speaker B (see Fig. 3) of type BMS 4599HE with a single tone and an amplitude of the incoming plane wave (downstream, if excited by speaker A, upstream, if excited by speaker B) in the corresponding hard walls section of 110 dB. The decomposed sound field prior and after the test section is used to determine the scattering coefficients (reflection R, transmission T, dissipation Δ) upstream and downstream of the channel with the tested resonator installed at one side of the duct. The test facility offers the possibility to measure the effect of grazing flow and nonlinear sound excitation with sound amplitudes of more than 130 dB; however, this was not investigated in this study. The facility has been extensively used for liner measurements and impedance eductions with a low error (< 3 %) in derived dissipation [21, 34, 35]. Figure 4 shows the experimental setup to validate the models introduced in Sections II and III. The subject of interest is a single modular Helmholtz resonator with one main cavity which can be extended on every outer side (each of the side walls and the back wall) with a flexible clamped plate inside a plate holder. The main cavity with a quadratic cross sectional area of $A_{\mathrm{cav}} = 35\,\mathrm{mm} \times 35\,\mathrm{mm}$ and a depth of $l_{\mathrm{cav}_1} = 60\,\mathrm{mm}$ is attached to a perforated facesheet with a thickness of 2 mm. The whole resonator system is flush mounted to the DUCT-R. The resonator has 18 evenly spaced orifices with a radius of $r_{\mathrm{neck}} = 0.75\,\mathrm{mm}$ and the open area ratio σ is 2.6 %. The regular cavity walls are made of aluminum. In this setup, the back wall was replaced by a plate holder with a flexible circular thermoplastic plate, followed by a second cavity and rigid back wall (see Fig. 2). We chose this plate's material in order to make use of a high loss factor and a suitable flexural rigidity to ensure that the first eigenfrequency is in the investigated frequency range. The plate is clamped into a plate holder tightened by ten screws to a torque of 0.2 Nm to ensure that the plate is clamped on its boundaries. The depth of the second cavity can be

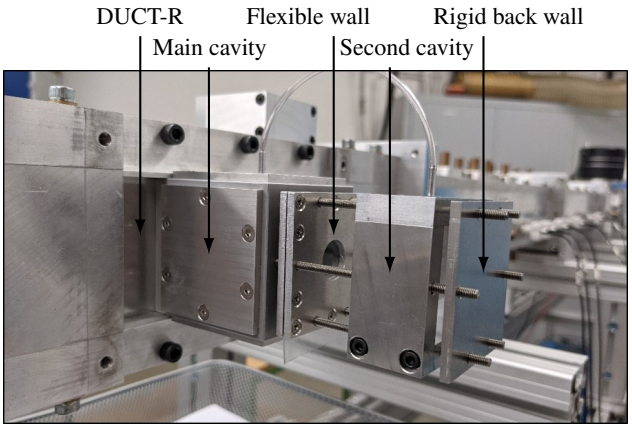

Fig. 4 Experimental setup to investigate Helmholtz resonators with flexible walls at the DUCT-R

Table 1 Properties of the experimental resonator

Cavity dimensions			Plate properties		
l_{cav_1}	=	60 mm	E	=	16 MPa
l_{cav_2}	=	25 mm	η	=	0.1
A_{cav}	=	35 mm×35 mm	ρ_{p}	=	1080 kg/m^3
l_{neck}	=	2 mm	ν_{PR}	=	0.48
r_{neck}	=	0.75 mm	h	=	0.3 mm
σ	=	2.6 %	R_{p}	=	7.5 mm
l_{PH}	=	4 mm			

varied. In this setup, a depth of $l_{\mathrm{cav}_2} = 25$ mm was chosen. Additionally, a thin hose (diameter 0.5 mm) connects both cavities to ensure that there is no static pressure difference during grazing flow measurements, similar to a static pressure equalization vent of a microphone. Further properties of the investigated resonator are listed in Table 1. This setup enables an investigation of a wide range of parameters including different materials of the flexible plate and different cavity dimensions. The simplest configuration is a SDOF Helmholtz resonator with one rectangular cavity with a depth of $l_{\mathrm{cav}} = 50$ mm. Note that this depth is smaller than l_{cav_1}.

We furthermore measured the scattering coefficients of a liner with multiple locally reacting resonators to validate the applicability of the Helmholtz resonator model (Section II) which forms the basis of the coupled resonator model (Section III). The liner (HRS1b) is a generic Helmholtz resonator liner, which consists of an aluminum perforated facesheet (opening diameter: 1 mm, perforation ratio: 1.8 %, thickness: 1 mm), tubes of polycarbonate as cells (length: 38.8 mm, diameter: 6.9 mm) and a solid back plate. The specific geometrical properties are the same as in [35] with the sole difference that the liner has a shorter axial length of 220 mm.

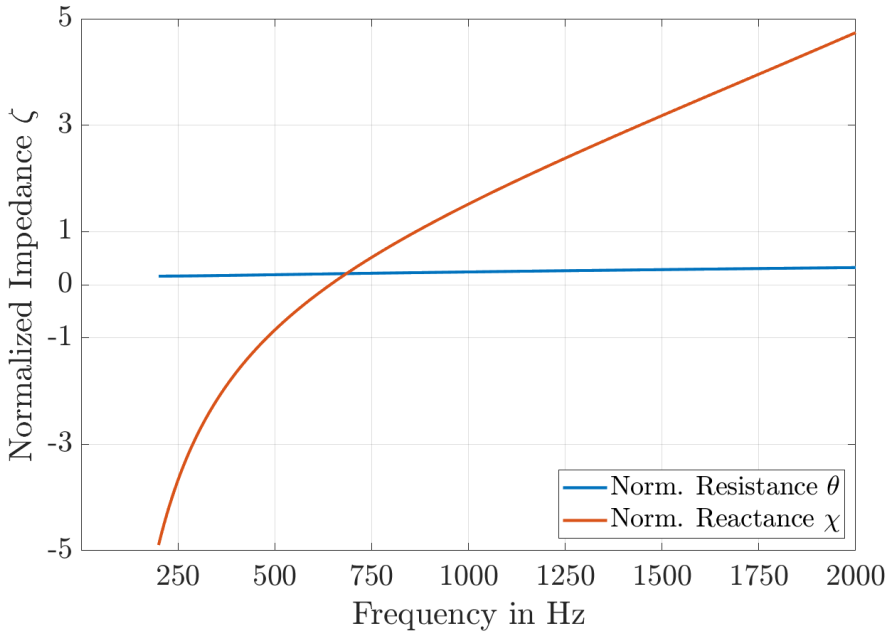

Fig. 5 Predicted normalized impedance $\zeta = \theta + \mathrm{i}\chi$ of the Helmholtz resonator

V. Results and Discussion

Figure 5 shows the predicted normalized impedance of the simple Helmholtz resonator versus the frequency. In this case, the main cavity is backed by a rigid back wall. The complex impedance $\zeta = Z/\rho_0\, c = \theta + \mathrm{i}\chi$, normalized by the specific acoustic impedance of air $\rho_0\, c$, is calculated with the model in Section II and can be described by the normalized resistance θ and the normalized reactance χ.

The single resonance is clearly visible around 600 Hz at the zero-crossing of the reactance (red). The resistance (blue) stems from the viscothermal losses and increases slightly towards higher frequencies. This predicted impedance is used as a boundary condition when solving the convective Helmholtz equation by finite differences with the code introduced in [36] to determine the scattering coefficients of the channel section. To compare the numerical results with the measurements, the predicted impedance is averaged with the hard wall area besides the resonator to create an effective channel impedance across the test section.

In Section II the viscothermal boundary layers inside the cavity are taken into account. Figure 6a shows the resistance of the cavity with consideration of different boundary layers. When all boundary layers are neglected, the cavity contributes no resistance (green). When the effect of the viscothermal boundary layer inside the cavity is taken into account, the cavity dissipates energy expressed by positive resistance. This can be modeled either by the approximation by Zwikker-Kosten (see [37], blue) or by Eq. (2) (red, dotted) which in the current case coincide, as the cavity is sufficiently wide and the "Kirchhoff 'wide tube'" approximation holds. The contribution f the viscothermal boundary layer is greater at lower shear wave numbers (thinner cavities or lower frequencies). Finally, the thermal boundary layer

of the back wall is added, resulting in the yellow line. Again, the contribution is greater for lower frequencies and adds substantially to the overall resistance of the cavity.

The latter, however, is small compared to the total resistance of the resonator in this specific example. This is visible in Fig. 6b. The total resistance is dominated by the facesheet's resistance (blue), whis is much higher than the cavity's resistance (red) and the thermal boundary layer resistance (yellow). The resistance of the cavity is, nevertheless, significant for thin cavities and low frequencies. Note that these results are specific to the resonator geometry and depends for example on the cavity's width. Figure 7a depicts a comparison between the experimentally determined and

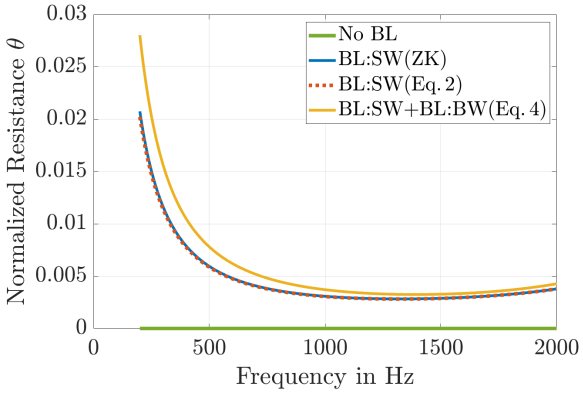

(a) Resistance of the cavity without considering boundary layers (green), with viscothermal side wall boundary layer according to Zwikker-Kosten (blue), with viscothermal side wall boundary layer according to Eq. (2) (red, dotted) and with viscothermal side wall boundary layer and thermal layer at back wall (orange). Note, that the blue and red line coincide.

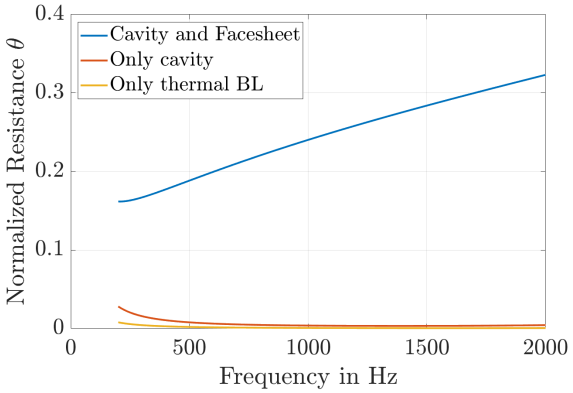

(b) Resistance of the whole resonator (blue), of the resonator cavity (red) and the the thermal boundary layer individually (yellow)

Fig. 6 Contribution of the cavity's boundary layers to the resonators' resistance

simulated scattering coefficients of the channel section with one Helmholtz resonator cell installed.

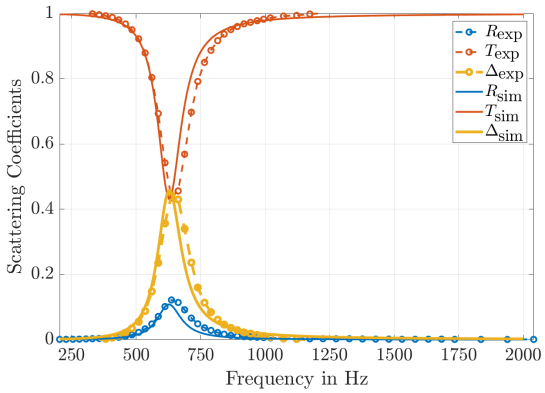

(a) Single Helmholtz resonator

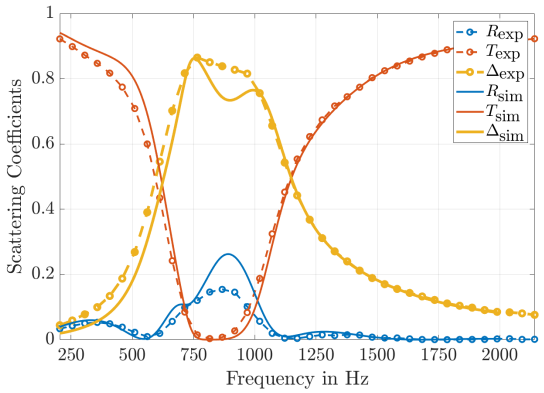

(b) Helmholtz resonator liner

Fig. 7 Comparison between measured (exp) and predicted (sim) scattering coefficients of the channel segment with a) single Helmholtz resonator and b) Helmholtz resonator liner: R reflection, T transmission, Δ dissipation

Both, reflection and transmission agree reasonably well. The same holds for the dissipation, as it is derived from the reflection and transmission coefficient. The model correctly predicts the damping amplitude of the single Helmholtz resonator. Nevertheless, all simulated curves seem to be slightly shifted towards lower frequencies. This may due to further multi-orifice effects, not yet correctly captured in the model in Section II. The dissipation appears to be small overall; however, one has to keep in mind that only the dissipation of a single Helmholtz resonator is shown. Additionally, the resonator was not constructed for optimal damping but for adaptability for future parameter studies.

Additionally, the model for the simple Helmholtz resonator introduced in Section II was used to predict the scattering coefficients of a liner with multiple locally reacting cells. A comparison between measured and predicted scattering coefficients is presented in Fig. 7b. Again, prediction and measurement agree very well. However, at the resonance around 850 Hz the energy reflection is mildly overpredicted. Note that $\Delta = 1 - R - T$ and as a consequence the dissipation is underpredicted around 900 Hz. This might stem from nonlinear effects such as jet formation at the openings, which suggests that a liner with a perforation ratio of 1.8 % exited by an acoustic pressure wave with an amplitude of 110 dB already shows amplitude dependent behavior.

The predicted normalized impedance of the Helmholtz resonator with a second cavity coupled by a flexible plate is depicted in Fig. 8. The impedance was calculated with the model introduced in Section III. Note that only the frequency range up to 1000 Hz is shown to see the effect of the flexible plate more clearly.

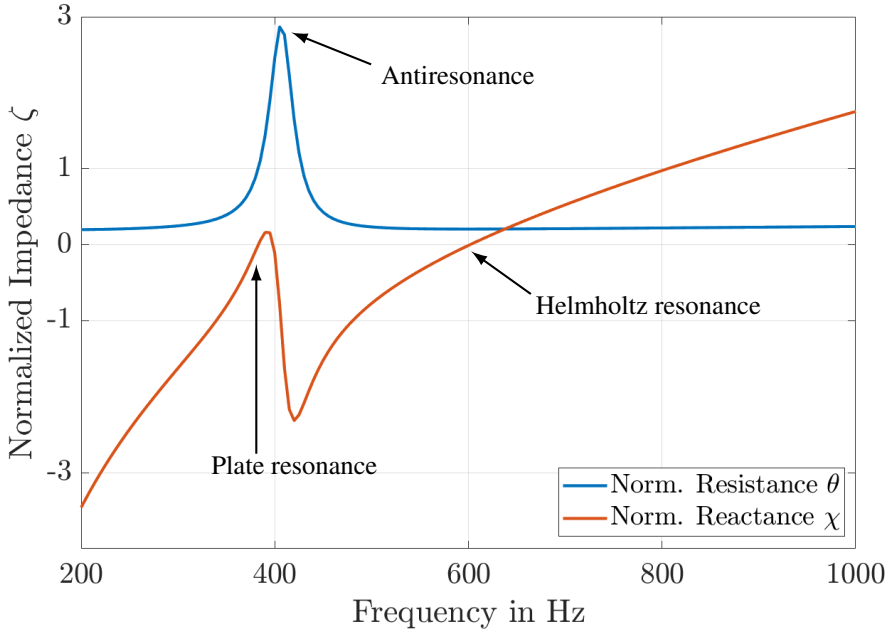

Fig. 8 Predicted normalized impedance $\zeta = \theta + \mathrm{i}\chi$ of the Helmholtz resonator with a flexible plate and a second cavity

Multiple zero-crossings of the reactance (red) are visible. The first zero-crossing around 380 Hz can be attributed to

the plate resonance. The peak of the resistance (blue) around 450 Hz stems from the antiresonance located between the plate resonance and the Helmholtz resonance around 600 Hz. The antiresonance is also visible as a zero-crossing of the reactance with negative slope.

The complex impedance $\zeta = \theta + \mathrm{i}\chi$ at different positions inside the cavity is shown in Fig. 9 to gain a better understanding of the coupling concept. The impedance of the second cavity θ_I, χ_I (dashed, Eq. (32)) is that of an tube

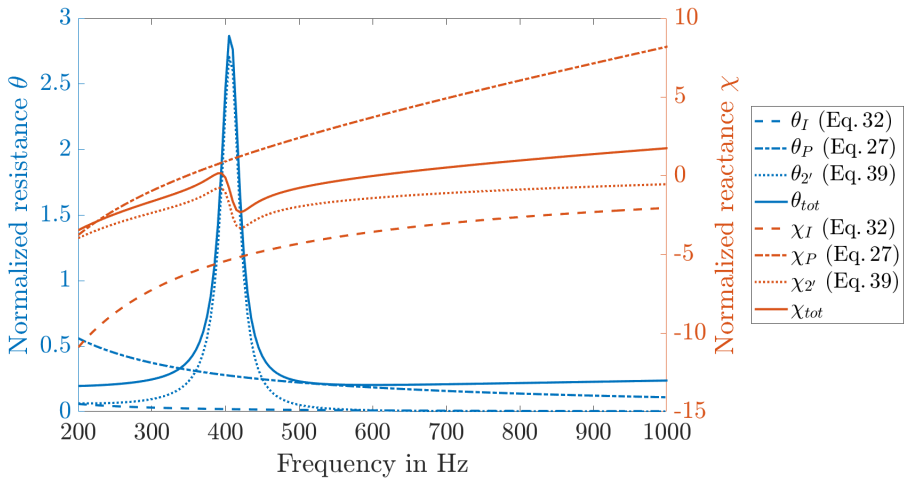

Fig. 9 Predicted normalized resistance (blue) and normalized reactance (red) of the Helmholtz resonator with a flexible plate and a second cavity of different contributors: θ_I, χ_I - dashed, second cavity (Eq. (32)); $\theta_\mathrm{P}, \chi_\mathrm{P}$ - dash-dotted, flexible plate (Eq. (27)); $\theta_{2'}, \chi_{2'}$ - dotted, main cavity and second cavity coupled by the flexible plate (Eq. (39)); $\theta_\mathrm{tot}, \chi_\mathrm{tot}$ - solid, total resonator impedance

with a small resistance at lower frequencies due to the viscothermal and thermal boundary layers at the walls and a reactance of cotangent shape $\chi_I \approx -\cot(kl_{\mathrm{cav}_2})$. The first geometrical resonance at a quarter wavelength of the second cavity alone $\chi_I = 0$ is out of the plotted frequency range due to its small length.

The impedance of the flexible plate (only considering the first mode, $\theta_\mathrm{P}, \chi_\mathrm{P}$ (dash-dotted, Eq. (27)) has a resistance which is highest for lower frequencies but significantly larger than that of the second cavity. The resistance stems from the material losses inside the flexible plate which are taken into account by its complex stiffness ($K_1 \in \mathbb{C}$). As presented in Eq. (27), the reactance of the flexible plate is a combination of its modal stiffness (K_1) and its modal mass (M_1). The stiffness is the dominant factor for low frequencies below the eigenfrequency. The mass of the flexible plate on the other hand is the dominant contributor for higher frequencies as the reactance approaches a linear slope with respect to the frequency. The eigenfrequency of the flexible plate in vacuo is visible at the zero crossing of the reactance $\chi_\mathrm{P} = 0$ around 350 Hz. The impedance of the main cavity and second cavity coupled by the flexible plate $\theta_{2'}, \chi_{2'}$ (dotted, Eq. (39)) is the normalized impedance inside the cavity just behind the facesheet. This impedance curve displays multiple resonances and the anti resonance in between. Note that the flexible plate and the second cavity (without the main cavity) already show multiple resonances (acting as a plate resonator), however, at much higher

frequencies (not shown here). Finally, the total resonator impedance $\theta_{\text{tot}}, \chi_{\text{tot}}$ (solid) is shown to highlight the effect of the facesheet. The facesheet adds resistance and reactance to the total resonator impedance ($\theta_{\text{tot}}, \chi_{\text{tot}}$ - solid). This, consequently, decreases the resonance frequency of both resonance frequencies associated with the plate resonance and the Helmholtz resonance. The total resonator impedance therefore is a sophisticated combination of multiple parameters which all contribute to its damping behavior.

In the following the results for the Helmholtz resonator coupled with a second cavity by a flexible plate modelled with the proposed model in Section III are presented. In Fig. 10 we see that the measured and simulated scattering coefficients of the channel section equipped with the coupled Helmholtz resonator agree reasonably well.

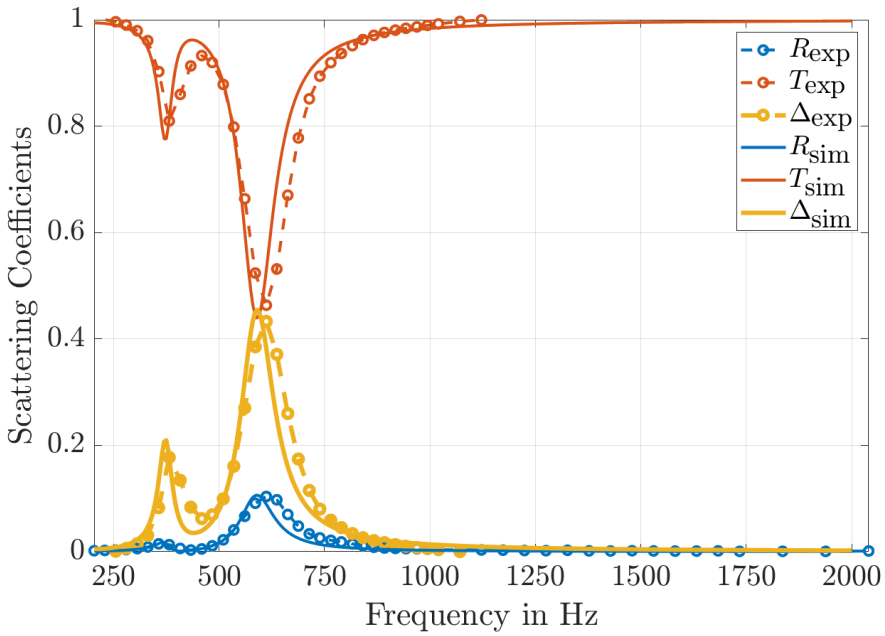

Fig. 10 Comparison between measured (exp) and predicted (sim) scattering coefficients of the section with the single Helmholtz resonator with a second cavity and a flexible plate: R reflection, T transmission, Δ dissipation

Both dissipation peaks are predicted correctly in their amplitude. Still, a similar frequency shift as the case of the simple Helmholtz resonator with multiple holes in Fig. 7a is visible. It is shown that the integration of a flexible plate in a resonator enables low-frequency damping – even lower than the Helmholtz resonance frequency. However, the peak due to the plate's resonance is comparably small. This may be due to the fact, that the area of the plate in the experiment was relatively small with respect to the cross section of the cavity. However, when using larger plates, multiple eigenmodes may be close to the Helmholtz resonance and the assumption of a single dominant eigenmode of the flexible plate may no longer hold.

The modular setup of the single Helmholtz resonator allows the investigation of different depths of the second cavity l_{cav_2}. We tested two additional cavity depths: $l_{\text{cav}_2} = 15\,\text{mm}$ (Fig. 11a, smaller) and $l_{\text{cav}_2} = 50\,\text{mm}$ (Fig. 11a, larger). It

is visible, that the Helmholtz resonance is not very sensitive with respect to the second cavity depth, as expected. On the contrary, the first damping resonance frequency associated with the plate resonance is altered when the depth of the second cavity is varied. The model is able to correctly predict the direction of these changes but, nevertheless, a shift between predicted and measured damping resonance is visible. This may due to unknown pre-stressing of the flexible plate during application, which alters the plate's elasticity.

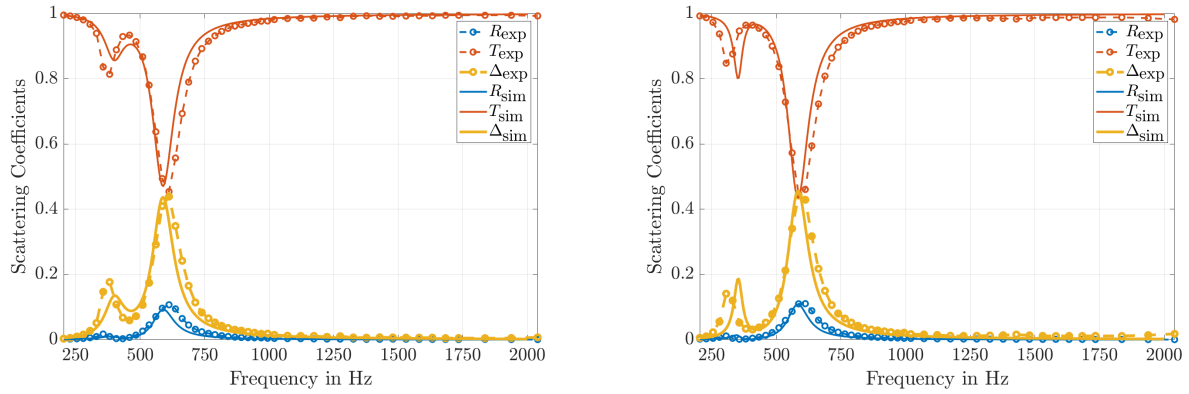

(a) Smaller second cavity with smaller depth (l_{cav_2} = 15 mm) **(b) Larger second cavity with more depth (l_{cav_2} = 50 mm)**

Fig. 11 Comparison between measured (exp) and predicted (sim) scattering coefficients of the section with the single Helmholtz resonator with a second cavity of variable depth and a flexible plate: R reflection, T transmission, Δ dissipation

The test facility offers the possibility to investigate the influence of a grazing flow on the acoustic behaviour of liners. The influence of a grazing flow (centerline Mach number of 0.1) and the connecting hose is depicted in Fig. 12. Neither influence is part of the analytic model and is therefore only briefly discussed. It is, nevertheless, important to evaluate the overall damping concept. The grazing flow has two effects on the dissipation of the resonator system: The first local maximum associated with the plate resonance is shifted to lower frequencies and the second local maximum associated with the Helmholtz resonator is slightly shifted towards higher frequencies, widened and decreased in amplitude. This is most likely due to the change of the facesheet impedance due to the grazing flow. However, it becomes apparent that a single resonator offers too little dissipation and a liner segment with multiple resonator cells is needed to investigate these grazing flow effects in greater detail.

The implementation of a hose to obtain a static pressure equilibrium between both cavities affects mainly the behavior of the plate under grazing flow conditions, as expected. When the second cavity is sealed (without the hose) the resonance is shifted towards higher frequencies. We assume that in this case the plate is statically deflected by the (not measured) static pressure difference.

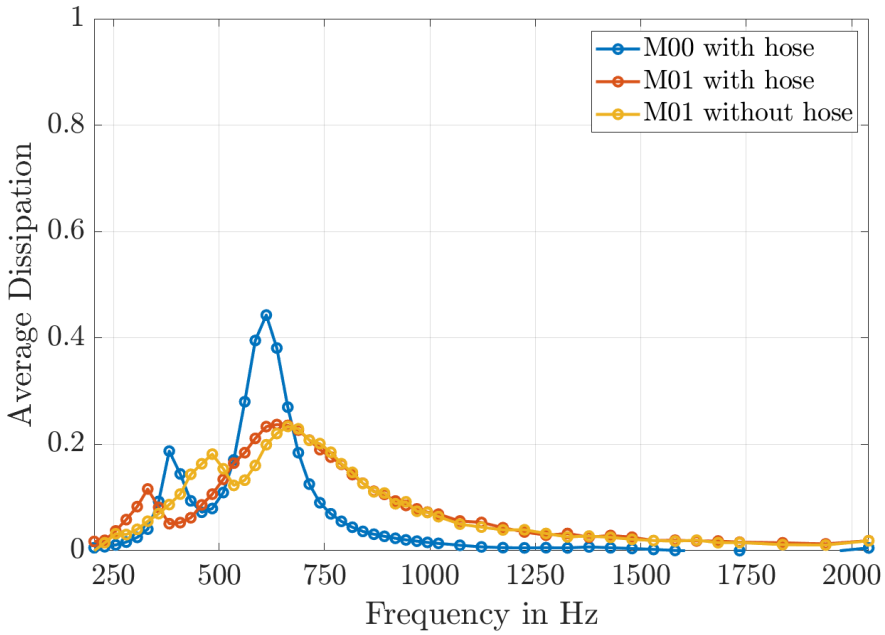

Fig. 12 Comparison between averaged dissipation of the lined duct section with the single Helmholtz resonator with a second cavity and a flexible plate without grazing flow (blue), with grazing flow and connecting hose (red) and with grazing flow but without connecting hose (yellow)

VI. Conclusions and Outlook

In this paper we proposed a novel modelling of a Helmholtz resonator with multiple necks and two cavities, coupled by a circular flexible plate. The model takes losses due to thermal conductivity (in the thermal boundary layer) and viscous damping (in the viscous boundary layer) inside the cavity and in the facesheet into account. Therefore all damping mechanisms of the Helmholtz resonator in the linear regime are included in the proposed model. When a flexible plate is used to subdivide the cavity, additional attenuation is introduced in the form of material damping. The clamped circular plate is modelled as an equivalent impedance of the first dominant mode and integrated into the Helmholtz resonator model. The predicted dissipation agreed well with experimental data of a single Helmholtz resonator chamber with multiple necks, both with and without a flexible plate, obtained at the DUCT-R test facility. The inclusion of a flexible plate allows the extension of the dissipation range of the system by multiple resonance peaks, even below the Helmholtz resonance. The dimensions of the flexible panel are constrained by the cavity's cross section, but the material can be tuned independently. Additionally, other properties such as the depth of both cavities, can be changed to tune the resonator. Consequently, the system's properties can be tuned towards low-frequency damping or broadband attenuation for a given volume. However, the resonances of the whole (system) are not the same as the sum of the individual resonances but mutually depend on each other. To gain more confidence, the model should be compared to different resonator geometries and liners with multiple resonators. For broader application, the effects of micro-perforations, grazing flow conditions, nonlinear sound excitation and different plate shapes with higher modes

need to be taken into account.

Acknowledgments

The authors would like to thank Julia Genßler for her assistance during the design and measurement of the experimental setup and Friedrich Bake for the fruitful discussions. This work is part of the project "Akustische Wirkmechanismen eines Helmholtz-Resonator-Liners mit flexiblen Strukturelementen" funded by the Deutsche Forschungsgemeinschaft (DFG, German Research Foundation) – 416728553 (EN 797/10-1). Their financial support is gratefully acknowledged.

References

[1] Sutliff, D. L., "Liner development at low technology readiness level utilizing the advanced noise control fan," *International Journal of Aeroacoustics*, Vol. 20, No. 5-7, 2021, pp. 680–707. https://doi.org/10.1177/1475472X211023836.

[2] Kinsler, L. F., Frey, A. R., Coppens, A. B., and Sanders, J. V., *Fundamentals of Acoustics*, 4th ed., John Wiley & Sons, Inc., New York, 2000, pp. 284–288.

[3] Ingard, U., "On the Theory and Design of Acoustic Resonators," *The Journal of the Acoustical Society of America*, Vol. 25, No. 6, 1953, pp. 1037–1061. https://doi.org/10.1121/1.1907235.

[4] Jones, M. G., Nark, D. M., and Howerton, B. M., "Impedance eduction for uniform and multizone acoustic liners," *International Journal of Aeroacoustics*, Vol. 20, No. 5-7, 2021, pp. 458–477. https://doi.org/10.1177/1475472X211023855.

[5] Jones, M. G., Simon, F., and Roncen, R., "Broadband and Low-Frequency Acoustic Liner Investigations at NASA and ONERA," *AIAA Journal*, 2022, pp. 1–20. https://doi.org/10.2514/1.J060862.

[6] Sutliff, D. L., Nark, D. M., and Jones, M. G., "Multi-degree-of-freedom liner development: Concept to flight test," *International Journal of Aeroacoustics*, Vol. 20, No. 5-7, 2021, pp. 792–825. https://doi.org/10.1177/1475472X211023860.

[7] Jones, M., Howerton, B., and Ayle, E., "Evaluation of Parallel-Element, Variable-Impedance, Broadband Acoustic Liner Concepts," AIAA-2012-2194, June 2012. https://doi.org/10.2514/6.2012-2194.

[8] L. W. Dean, "Coupling of Helmholtz Resonators to Improve Acoustic Liners for Turbofan Engines at Low Frequency," NASA-CR-134912, August 1975. URL https://ntrs.nasa.gov/search.jsp?R=19760014122.

[9] Xu, M. B., Selamet, A., and Kim, H., "Dual Helmholtz resonator," *Applied Acoustics*, Vol. 71, No. 9, 2010, pp. 822–829. https://doi.org/10.1016/j.apacoust.2010.04.007.

[10] Tang, S. K., Ng, C. H., and Lam, E., "Experimental investigation of the sound absorption performance of compartmented Helmholtz resonators," *Applied Acoustics*, Vol. 73, No. 9, 2012, pp. 969–976.

[11] Mechel, F. P., *Sound Absorbers: Inner Sound Fields [Original in German: "Schallabsorber: Innere Schallfelder - Strukturen"]*, Hirzel, Stuttgart, 1995, Schallabsorber, Vol. 2, pp. 767–771.

[12] Cremer, L., Heckl, M., and Petersson, B. A. T., *Structure-borne sound: Structural vibrations and sound radiation at audio frequencies,*, 3rd ed., Springer, Berlin, 2005, pp. 119–120. https://doi.org/10.1007/b137728.

[13] Griffin, S., Lane, S. A., and Huybrechts, S., "Coupled Helmholtz Resonators for Acoustic Attenuation," *Journal of Vibration and Acoustics*, Vol. 123, No. 1, 2001, pp. 11–17. https://doi.org/10.1115/1.1320812.

[14] Zhao, D., "Transmission Loss Analysis of a Parallel-Coupled Helmholtz Resonator Network," *AIAA Journal*, Vol. 50, No. 6, 2012, pp. 1339–1346. https://doi.org/10.2514/1.J051453.

[15] Mi, Y., and Yu, X., "Attenuation of low-frequency sound in U-shaped duct with membrane coupled acoustic resonator: Modeling and analysis," *Journal of Sound and Vibration*, Vol. 489, 2020, p. 115679. https://doi.org/10.1016/j.jsv.2020.115679.

[16] Dodge, C., Zhang, Y., Cattafesta, L. N., Howerton, B. M., and Kreitzman, J. R., "A Dielectric Elastomer Acoustic Liner," AIAA AVIATION 2021 Forum, August 2021. https://doi.org/10.2514/6.2021-2244.

[17] Horowitz, S. B., Nishida, T., Cattafesta, L. N., and Sheplak, M., "Characterization of a Compliant-Backplate Helmholtz Resonator for an Electromechanical Acoustic Liner," *International Journal of Aeroacoustics*, Vol. 1, No. 2, 2002, pp. 183–205. https://doi.org/10.1260/147547202760236969.

[18] Liu, F., Horowitz, S., Nishida, T., Cattafesta, L., and Sheplak, M., "A multiple degree of freedom electromechanical Helmholtz resonator," *The Journal of the Acoustical Society of America*, Vol. 122, No. 1, 2007, pp. 291–301. https://doi.org/10.1121/1.2735116.

[19] Nudehi, S. S., Duncan, G. S., and Farooq, U., "Modeling and Experimental Investigation of a Helmholtz Resonator with a Flexible Plate," *Journal of Vibration and Acoustics*, Vol. 135, No. 4, 2013. https://doi.org/10.1115/1.4023810.

[20] Knobloch, K., Enghardt, L., and Bake, F., "Helmholtz Resonator Liner with Flexible Walls," AIAA-2018-4102, June 2018. https://doi.org/10.2514/6.2018-4102.

[21] Knobloch, K., Enghardt, L., and Bake, F., "Investigation of Flexible Walls for Acoustic Liners," AIAA-2019-2565, June 2019. https://doi.org/10.2514/6.2019-2565.

[22] Liu, G.-S., Peng, Y.-Y., Liu, M.-H., Zou, X.-Y., and Cheng, J.-C., "Broadband acoustic energy harvesting metasurface with coupled Helmholtz resonators," *Applied Physics Letters*, Vol. 113, No. 15, 2018. https://doi.org/10.1063/1.5041731.

[23] Sanada, A., and Tanaka, N., "Extension of the frequency range of resonant sound absorbers using two-degree-of-freedom Helmholtz-based resonators with a flexible panel," *Applied Acoustics*, Vol. 74, No. 4, 2013, pp. 509–516. https://doi.org/10.1016/j.apacoust.2012.09.012.

[24] Schulz, A., "Die akustischen Randbedingungen perforierter Wandauskleidungen in Strömungskanälen: Physikalische Modelle und Eduktion, [Translated title: The acoustic boundary conditions of perforated walls in ducts: physical models and eduction]," Ph.D. thesis, Technische Universität Berlin, Berlin, 2019. https://doi.org/10.14279/depositonce-7943.

[25] Schulz, A., Bake, F., Enghardt, L., and Ronneberger, D., "Impedance Eduction of Acoustic Liners Based on Four Different Levels of Physical Modeling," AIAA-2016-2726, June 2016. https://doi.org/10.2514/6.2016-2726.

[26] Cremer, L., "Über die akustische Grenzschicht vor starren Wänden [Translated title: About the acoustic boundary layer in front of rigid walls]," *Archiv der elektrischen Übertragung*, Vol. 2, 1948, pp. 136–139.

[27] Tijdeman, H., "On the propagation of sound waves in cylindrical tubes," *Journal of Sound and Vibration*, Vol. 39, No. 1, 1975, pp. 1–33. https://doi.org/10.1016/S0022-460X(75)80206-9.

[28] Kirchhoff, G., "About the influence on thermal conductivity of a gas with respect to sound movement [Original in German: Ueber den Einfluss der Wärmeleitung in einem Gase auf die Schallbewegung]," *Annalen der Physik und Chemie*, Vol. 210, No. 6, 1868, pp. 177–193. https://doi.org/10.1002/andp.18682100602.

[29] Fock, V. A., "A Theoretical Investigation of the Acoustical Conductivity of a Circular Aperture in a Wall put across a Tube," *Comptes Rendus (Doklady) de l'Académie des Sciences de l'URSS*, Vol. Volume XXXI, No 9, 1941, pp. 875–878.

[30] Blevins, R. D., *Formulas for dynamics, acoustics and vibration*, Wiley series in acoustics noise and vibration, Wiley, Chichester (UK), 2016. https://doi.org/10.1002/9781119038122.

[31] Leissa, A. W., and Narita, Y., "Natural frequencies of simply supported circular plates," *Journal of Sound and Vibration*, Vol. 70, No. 2, 1980, pp. 221–229. https://doi.org/10.1016/0022-460X(80)90598-2.

[32] Chung, J. Y., "Rejection of flow noise using a coherence function method," *The Journal of the Acoustical Society of America*, Vol. 62, No. 2, 1977, pp. 388–395. https://doi.org/10.1121/1.381537.

[33] Lahiri, C., "Acoustic Performance of Bias Flow Liners in Gas Turbine Combustors," Ph.D. thesis, Technische Universität Berlin, Berlin, 2014. https://doi.org/10.14279/depositonce-4270.

[34] Lahiri, C., Enghardt, L., Bake, F., Sadig, S., and Gerendás, M., "Establishment of a High Quality Database for the Acoustic Modeling of Perforated Liners," *Journal of Engineering for Gas Turbines and Power*, Vol. 133, No. 9, 2011. https://doi.org/10.1115/1.4002891.

[35] Busse-Gerstengarbe, S., Bake, F., Enghardt, L., and Jones, M. G., "Comparative Study of Impedance Eduction Methods, Part 1: DLR Tests and Methodology," AIAA-2013-2124, May 2013. https://doi.org/10.2514/6.2013-2124.

[36] Weng, C., Enghardt, L., and Bake, F., "Comparison of Non-Modal-Based and Modal-Based Impedance Eduction Techniques," AIAA-2018-3773, June 2018. https://doi.org/10.2514/6.2018-3773.

[37] Parrott, T. L., and Jones, M. G., "Parallel-element liner impedances for improved absorption of broadband sound in ducts," *Noise Control Engineering Journal*, Vol. 43, No. 6, 1995, p. 183. https://doi.org/10.3397/1.2828379.